Journal of Power Sources 684 (2026) 240417

Contents lists available at ScienceDirect

Journal of Power Sources

journal homepage: www.elsevier.com/locate/jpowsour

Designing high-performance supercapacitors with indirubin-derived dynamic conjugated microporous polymers

Mohammed G. Kotp [a,b], Shiao-Wei Kuo [a,c,*]

[a] Department of Materials and Optoelectronic Science, Center for Functional Polymers and Supramolecular Materials, National Sun Yat-Sen University, Kaohsiung, 80424, Taiwan
[b] Interdisciplinary Research Center for Advanced Materials (IRC-AM), King Fahd University of Petroleum and Minerals, Dhahran, 31261, Saudi Arabia
[c] Department of Medicinal and Applied Chemistry, Kaohsiung Medical University, Kaohsiung, 807, Taiwan

HIGHLIGHTS

- Indirubin-based CMPs were developed for supercapacitor electrodes.
- TPA-BD CMP outperforms Py-BD CMP *via* stronger pseudocapacitive charge storage.
- TPA-BD CMP reaches 916.6 F g^{-1} at 1 A g^{-1} in aqueous electrolyte.
- A symmetric TPA-BD CMP coin cell delivers 232.5 F g^{-1} at 1 A g^{-1}.
- The device maintains 79.4% of its capacitance after 10,000 cycles.

GRAPHICAL ABSTRACT

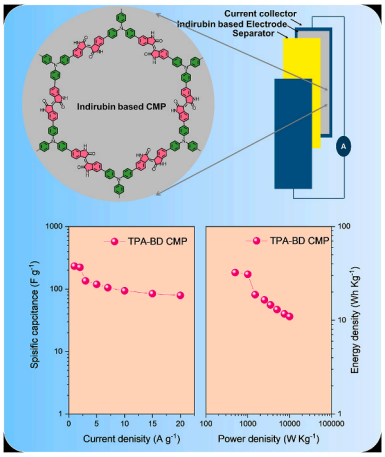

ARTICLE INFO

Keywords:
Conjugated microporous polymers (CMPs)
Indirubin derivatives
Supercapacitors
Energy storage
Redox activity

ABSTRACT

We develop and analyze the conjugated microporous polymers (CMPs), Py-BD and TPA-BD CMPs, incorporating indirubin-based units for enhanced energy storage applications. The Py-BD CMP exhibits a higher surface area up to 250 m^2 g^{-1}, superior thermal stability as evidenced by a higher decomposition temperature up to 434.6 °C in thermal gravimetric analysis (TGA). On the other hand, TPA-BD CMP displays a higher capacitance per unit mass of 916.5 F g^{-1} at 1 A g^{-1} compared to Py-BD CMP. We conduct electrochemical evaluations using a two-electrode coin cell system with TPA-BD CMP, which demonstrates high capacitance and stability of 232.50 F g^{-1} and 83% respectively after 5000 cycles. The TPA-BD CMP-based coin cell shows promising performance, highlighting its

* Corresponding author. Department of Materials and Optoelectronic Science, Center for Functional Polymers and Supramolecular Materials, National Sun Yat-Sen University, Kaohsiung, 80424, Taiwan.
E-mail address: kuosw@faculty.nsysu.edu.tw (S.-W. Kuo).

https://doi.org/10.1016/j.jpowsour.2026.240417
Received 28 October 2025; Received in revised form 29 April 2026; Accepted 15 May 2026
Available online 18 May 2026

suitability as an advanced and active material for supercapacitors. Our findings contribute to the development of advanced energy storage performance through the unique features of indirubin derivatives in CMP architectures.

1. Introduction

The quest for efficient and sustainable energy storage solutions are now more important than ever with the global shift to renewable energy as well seeks to mitigate the challenges posed by climate change [1–8]. Among the various technologies being explored, supercapacitors are showing as great potential candidates thanks to their ability to store and release electrical energy rapidly, making them ideal solutions for important applications such as electric vehicles [9–11]. A key component in the development of high-performance supercapacitors is the design of advanced electrode materials such as those innovated porous organic materials that are able to enhance or modulate energy density, power density, and overall efficiency [12–16].

On the other hand, conjugated microporous polymers (CMPs) have drawn significant interest lately owing to their unique structural features, which include high surface areas, tunable pore sizes, and excellent chemical stability [17–24]. These fruitful features make CMPs particularly suitable for energy storage devices, as they can efficiently facilitate ions transport and provide a robust framework for charge storage [17, 25–29]. Among the diverse range of CMPs being developed, those based on indirubin derivatives have not discovered or shown their remarkable potential yet. Realistically, indirubin, a natural compound known for its biological activity, has been adapted into various chemical structures for energy storage applications [30–33].

Indirubin molecules, known for their planar structure and inherent redox properties, have been extensively studied for their therapeutic applications, particularly in combating proliferative diseases such as cancer and psoriasis [30,34]. Beyond their biological significance, indirubin derivatives have shown potential in various technological applications due to their chemical stability and ability to undergo redox transformations [35,36]. The integration of indirubin units into CMPs offers a novel approach toward leveraging these properties for energy storage applications. By incorporating indirubin-based moieties into CMP architectures, researchers can exploit their redox activity to enhance pseudocapacitance and overall electrochemical performance, thereby may contribute toward the development of advanced supercapacitor materials. Specifically, the (E)-[3,3′-biindolinylidene]-2, 2′-dione (BD) moiety has not been well-studied previously as a building block for CMPs although its expected inherent redox activity and stability.

We here focus on the development and characterization of two CMPs, Py-BD and TPA-BD CMPs, which incorporate indirubin-based BD units into their structures. By integrating these units with boronated forms of pyrene (Py-4Bor) and triphenylamine (TPA-3Bor), respectively, we aim to rise and modulate the unique electronic and structural properties of these monomers to enhance the electrochemical performance of the resulting CMPs. Actually, Py and TPA moieties record high reputation as CMP blocks utilize as supercapacitor electrodes [37–40]. Therefore, the Py-BD and TPA-BD CMPs are designed to exploit the synergistic effects of their constituent components, combining the high surface area and conductivity of CMPs with the redox activity of indirubin derivatives. This approach is expected to yield porous materials with improved capacitive behavior, higher energy density, and enhanced cycling stability, making them well-suited for advanced energy storage applications.

We deeply investigated their surface chemical composition and thermal stability using X-ray photoelectron spectroscopy (XPS), and thermal gravimetric analysis (TGA) respectively. Moreover, the surface area of those innovative BD CMPs records up to 250 $m^2 g^{-1}$. Additionally, through a comprehensive analysis of their electrochemical properties, including cyclic voltammetry (CV), galvanostatic charge-discharge (GCD) measurements, and electrochemical impedance spectroscopy (EIS), we evaluate the performance of Py-BD and TPA-BD CMPs as supercapacitor electrodes. The capacitance of the three electrode and double electrode systems records up to 916.55 and 232.50 $F g^{-1}$ respectively at 1 $A g^{-1}$. The findings of this study provide a deeper understanding regarding the potential of indirubin-based CMPs for energy storage systems, highlighting their advantages and challenges in the context of emerging energy technologies.

2. Experimental section

2.1. Materials

All chemicals utilized in our experiments were of analytical grade and used as received. Additionally, We employed double-distilled water in all procedures. Isatin, potassium borohydride (KBH_4), and pyrene were provided from Sigma Aldrich. Nitrobenzene, bromine, methanol (CH_3OH), ethanol (C_2H_5OH), dioxane, dimethylformamide (DMF), and dichloromethane (DCM) were from Thermo Fisher. Bis(pinacolato) diboron [1,1′ bis(diphenylphosphino)ferrocene] dichloropalladium(II) (Pd(dppf)Cl_2), triphenylamine, N-bromosuccinimide (NBS), tetrakis (triphenylphosphine)palladium(0) ($Pd(PPh_3)_4$), potassium carbonate (K_2CO_3), carbon black, Nafion (10% wt%), and potassium hydroxide (KOH) were purchased from Acros. The synthesis of Pyrene-4Bor and TPA-3Bor was described in the supporting information.

2.2. The synthesis of BD-2Br

The (E)-6,6'-dibromo-[3,3'-biindolinylidene]-2,2'-dione (BD-2Br) was designed as schemed early [41]. The 6-bromoindoline-2,3-dione (0.01 mol) was solubilized in 50 mL of methanol (CH_3OH) in a 150 mL round-bottom flask set up with a reflux condenser and stirring bar. The mixture was subjected to heat under reflux, and KBH_4 (0.27 g, 0.005 mol) was added gradually. The reaction mixture was allowed to stir under reflux over 1 h. During this time, the stopper of the flask was removed 2-3 times, and the flask was gently shaken to ensure the reaction mixture was saturated with air. After 1 h, the solution was left to reach room temperature, resulting in the precipitation of BD-2Br. The product was then obtained *via* filtration and further purified through recrystallization from 95% ethanol (C_2H_5OH).

2.3. The synthesis of Py-BD CMP

Utilizing Suzuki coupling protocol [42,43], those as-synthesized monomers of BD-2Br (200 mg, 0.47 mmol) and Py-4Bor (168 mg, 0.23 mmol) were combined in a Schlenk tube with $Pd(PPh_3)_4$ (55 mg, 0.04 mmol) and K_2CO_3 (658 mg, 4.7 mmol), followed by degassing for 15 min. A co-solvent mixture of DMF (10.34 mL) and water (1.3 mL) was then charged into the reaction tube. The feeding tube was subjected to a triple freeze-thaw cycles. The reaction proceeded under continuous stirring at 130 °C for 72 h. Afterward, the resulting polymer was isolated and thoroughly washed using Soxhlet extraction with methanol, hexane, acetone, and THF. Finally, The powder was oven-dried at 80 °C under vacuum.

2.4. The synthesis of TPA-BD CMP

The synthesis process followed the method used for Py-BD CMP, with TPA-3Bor substituted instead. The as-synthesized monomers of TPA-3Bor (197.8 mg, 0.31 mmol) and BD-2Br (200 mg, 0.47 mmol) were combined in a Schlenk tube with $Pd(PPh_3)_4$ (55 mg, 0.04 mmol) and

K_2CO_3 (658 mg, 4.7 mmol), and the mixture was degassed for 15 min. A co-solvent of DMF (10 mL) and water (1.25 mL) was then added, after which the feeding tube underwent a triple freeze-thaw cycle. The reaction was stirred continuously at 130 °C for 72 h. Following the reaction, the resultant polymer was centrifuged and thoroughly washed using Soxhlet extraction with methanol, hexane, acetone, and THF. Finally, the solid was oven-dried at 80 °C under vacuum.

2.5. Electrochemical performance evaluation

Prior to use, the glassy carbon electrode (GCE) was sonicated in a water bath for 30 min to ensure thorough cleaning. It was then polished with 0.05 μm alumina as well ethanol to ensure a smooth surface. Finally, the electrode was allowed to dry in air oven (60 °C).

Such electro-chemical performance of those BD CMPs was evaluated utilizing an Autolab potentiostat (PGSTAT204) in a 1 M KOH aqueous electrolyte. Realistically, 1 M KOH was selected because alkaline electrolytes are widely used in supercapacitor studies due to their high ionic conductivity and low internal resistance, which enable efficient ion transport and improved electrochemical performance. The working electrochemical electrode was GCE (diameter: 5.61 mm; 0.2475 cm^2), whilst a platinum wire functioned as the counter electrode. A Hg/HgO reference electrode (RE-1B, BAS) was utilized, with all potentials referenced to this electrode. For the preparation of the samples, equal 2 mg of both CMP was mixed with carbon black throughout 800 μL of aqua and 191 μL of ethanol, followed by sonication for 30 min. Subsequently, 9 μL of Nafion (10% wt%) was incorporated under ongoing sonication for an additional hour. The tip of the working electrode was modified by coating with 5 μL of the mixture, followed by drying under vacuum at 70 °C for 30 min.

Electrochemical features were assessed through CV experiments carried out at different scan rates ranging between 5:200 mV s^{-1} as well *via* the GCD method within a voltage range of 0: −0.7 V at current densities in-between 1:20 A g^{-1}. The specific capacitances of BD CMPs have calculated from the GCD data throughout Eq. (1).

$$C_p = \frac{I_m \, \Delta t}{m \, \Delta V} \quad \text{(Eq.1)}$$

In this context, C_p, I_m, Δt, m, and ΔV represent the specific capacitance, discharge current, discharge time, mass of CMP on the electrode, and potential drop, respectively. The densities of energy and power were respectively calculated using Eqs. (2) and (3).

$$E_g = \frac{1}{2} C_p (\Delta V)^2 \quad \text{(Eq.2)}$$

$$P = \frac{E_g}{\Delta t} \quad \text{(Eq.3)}$$

2.6. Coin cell assembly

A slurry of 70 wt% CMPs, 20 wt% carbon, and 10 wt% Nafion in 2 mL ethanol was used to prepare the working electrodes for the coin cells. The slurry was applied onto carbon foil subsequently cut into circular electrodes. Notably the working electrodes were prepared on flexible Torayca™ carbon paper (0.1 mm thickness) and cut into circular discs with a diameter of 1 cm. The mass loading of the active material on the current collector was approximately 1.27 mg cm^{-2}. The electrodes have been set up into a real coin supercapacitor, which included couple symmetric working electrodes, separator, as well as KOH electrolyte. The electrochemical behavior of the coin cells was assessed using CV experiments applying several scan rates ranging from 5:200 mV s^{-1}, as well as through the GCD method within potentials of −0.3: +0.6 V and current densities of 1:20 A g^{-1}. The GCD experiments were utilized to determine the capacitance of the device using Eq. (1)).

3. Results and discussion

3.1. Molecular characterization

Two novel indirubin-based CMPs, Py-BD and TPA-BD, were synthesized in high yields *via* the standard Suzuki coupling of the dibromo-functionalized linker BD-2Br with the boronic acid pinacol ester linkers Py-4Bor and TPA-3Bor, respectively. The reactions were carried out in a DMF/water co-solvent (10:1, v/v) at 130 °C using tetrakis(triphenylphosphine)palladium(0) as the catalyst, as illustrated in Scheme 1. The BD-CMPs were found to be insoluble in common solvents (methanol, ethanol, acetone, THF, and DMF), implying the formation of highly cross-linked chemical structures [44,45]. The as-synthesized BD-CMPs were first analyzed for their chemical composition using FTIR and solid-state ^{13}C CP/MAS NMR spectroscopy. Notably, FTIR scans of both Py-BD and TPA-BD CMPs show a full loss of the absorption signal at 827 cm^{-1}, which is associated with the C–Br linkage in the starting monomer of BD-2Br [42]. This absence confirms that the bromine functionalities have been fully consumed during the polymerization process, suggesting efficient coupling reactions between the monomers. Additionally, the B–O absorption signals at 1373 cm^{-1} and 1337 cm^{-1}, characteristic of the boronated units of Py-4Bor and TPA-3Bor, respectively, are no longer present [46]. This disappearance further supports the successful incorporation of these monomers into the CMP framework through the formation of new bonds. Interestingly, the FTIR records also reveal the emergence of new absorption bands that are characteristic of the structural features of the CMPs. Specifically, the signals at 1673 cm^{-1} and 1707 cm^{-1} are attributed to the C=O bonds of the indirubin units, indicating their successful integration into the CMP structure [41]. Furthermore, the signals at 1609 cm^{-1} and 1617 cm^{-1} correspond to the CN bonds within the indirubin moieties, while bands at 1473 cm^{-1} and 1493 cm^{-1} are associated with the aryl C=C bonds in Py-BD and TPA-BD CMPs, respectively (Fig. 1a). These observations collectively confirm the formation of the desired polymer structures through the coupling of the monomers. On the other hand, the NMR spectroscopy of those Py-BD and TPA-BD CMPs provided valuable insights into their molecular structure. The spectra revealed characteristic signals that can be attributed to specific functional groups within the polymers. Signals at 170.82 ppm and 157.10 ppm were observed for the C=O units (Fig. 1b). These chemical shifts are consistent with carbonyl groups, which are typically found in the range of 165-220 ppm for various carbonyl compounds such as ketones and aldehydes. The presence of these signals confirms the incorporation of carbonyl functionalities within the Py-BD and TPA-BD CMPs, which derived from the indirubin derivative used in their synthesis. The observed shifts in the C–N and C=O signals in the solid-state NMR spectra can be attributed to differences in the local electronic environments of the two CMPs. In particular, the presence of the electron-donating TPA unit can increase the electron density within the conjugated framework, which may lead to slight effects and thus shifts in the corresponding NMR peaks compared to the Py-based system. This behaviour suggests the existence of electronic interactions between the TPA unit and the indirubin core within the conjugated network. Such donor–acceptor interactions can facilitate partial charge transfer along the polymer backbone, enhancing electron delocalization. This effect is expected to contribute to the improved electrochemical performance observed for TPA-BD CMP, particularly through enhanced pseudocapacitive behaviour. Additional signals at 147.22 ppm and 152.72 ppm were assigned to the C-N units (Fig. 1b). These chemical shifts are indicative of carbon atoms bonded to nitrogen, which can be found in various nitrogenic units. The presence of these signals highlights the successful inclusion of nitrogenic moieties, such as those from triphenylamine in TPA-BD CMP, into the polymer structure. The range of signals from 120.35 ppm to 96.20 ppm can be attributed to the aromatic C=C units. These chemical shifts fall within the typical range for aromatic carbons, which are generally observed between 125 and 150 ppm (Fig. 1b). The presence of these

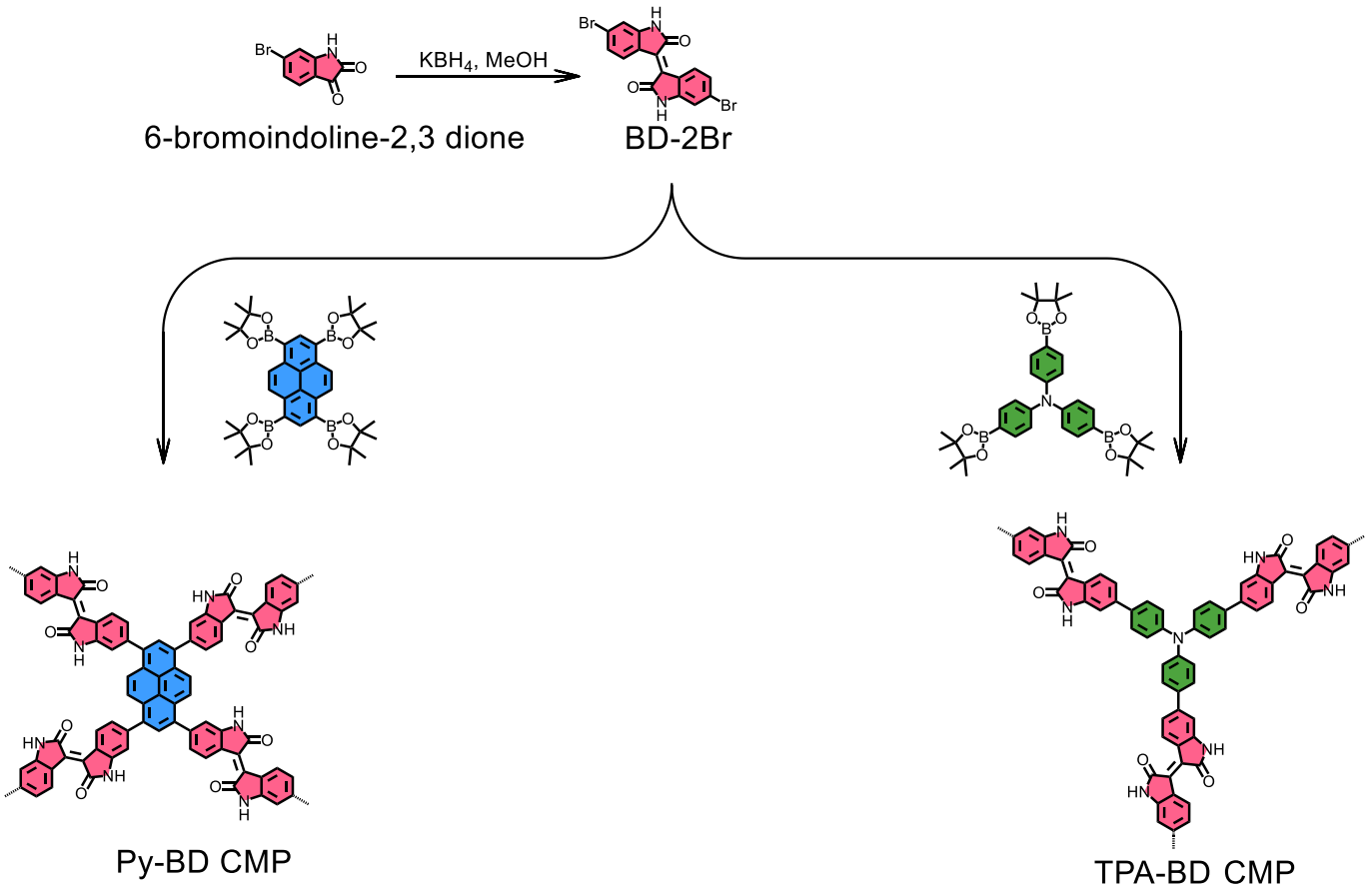

Scheme 1. Synthesis protocols of Py-BD and TPA-BD CMPs utilizing Suzuki coupling methodology.

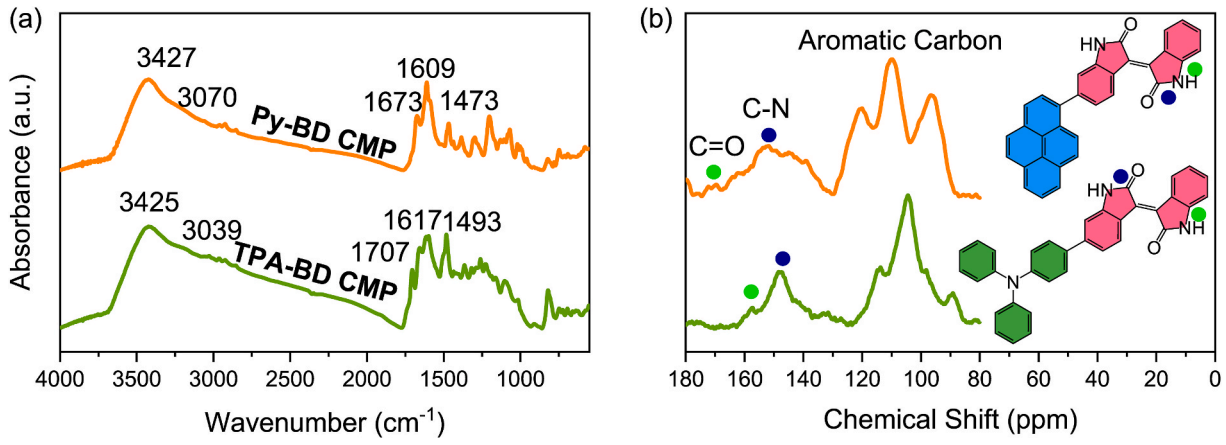

Fig. 1. (a) FTIR and (b) solid state NMR spectroscopy of Py-BD and TPA-BD CMPs.

signals confirms the aromatic nature of the polymer backbone, which is essential for the conjugated structure of these CMPs.

To elucidate the surface bonding environment and valence states of carbon, nitrogen, and oxygen in the Py-BD and TPA-BD CMPs, XPS measurements were conducted. The HR-XPS spectra for C1s, N1s, and O1s are presented in Fig. 2, providing detailed insights into the chemical environments within these polymers. The C1s spectra of both Py-BD and TPA-BD CMPs were deconvoluted into four distinct signals, revealing the presence of multiple carbon states (Fig. 2a). These include sp^2 carbons (C=C) at approximately 283.30 eV, sp^2 carbon-containing nitrogenic units (C=N) at 283.99 eV, and carbonaceous atoms attached to oxygen (C=O) at 284.45 eV [47,48]. Realistically, the identification of these carbon states is crucial for emphasizing the structural and electronic properties of those BD CMPs, as they reflect the extent of π-conjugation and functional group incorporation within the CMPs frameworks. The deconvolution of the N1s spectra for Py-BD and TPA-BD CMPs revealed distinct nitrogen states (Fig. 2b). In both CMPs, a peak centered at approximately 398.5 eV was observed, which is assignable to pyrrolic-N within the indirubin ring [49]. This N state may contribute one π-electron to the aromatic π-system, enhancing the electronic conductivity and redox activity of the CMPs [50,51]. Notably, the N1s spectrum of TPA-BD CMP also exhibited a characteristic peak at 397.07 eV, corresponding to the 3ry-N of the TPA subunit. Furthermore, the quantitative analysis indicated that pyrrolic-N is the dominant

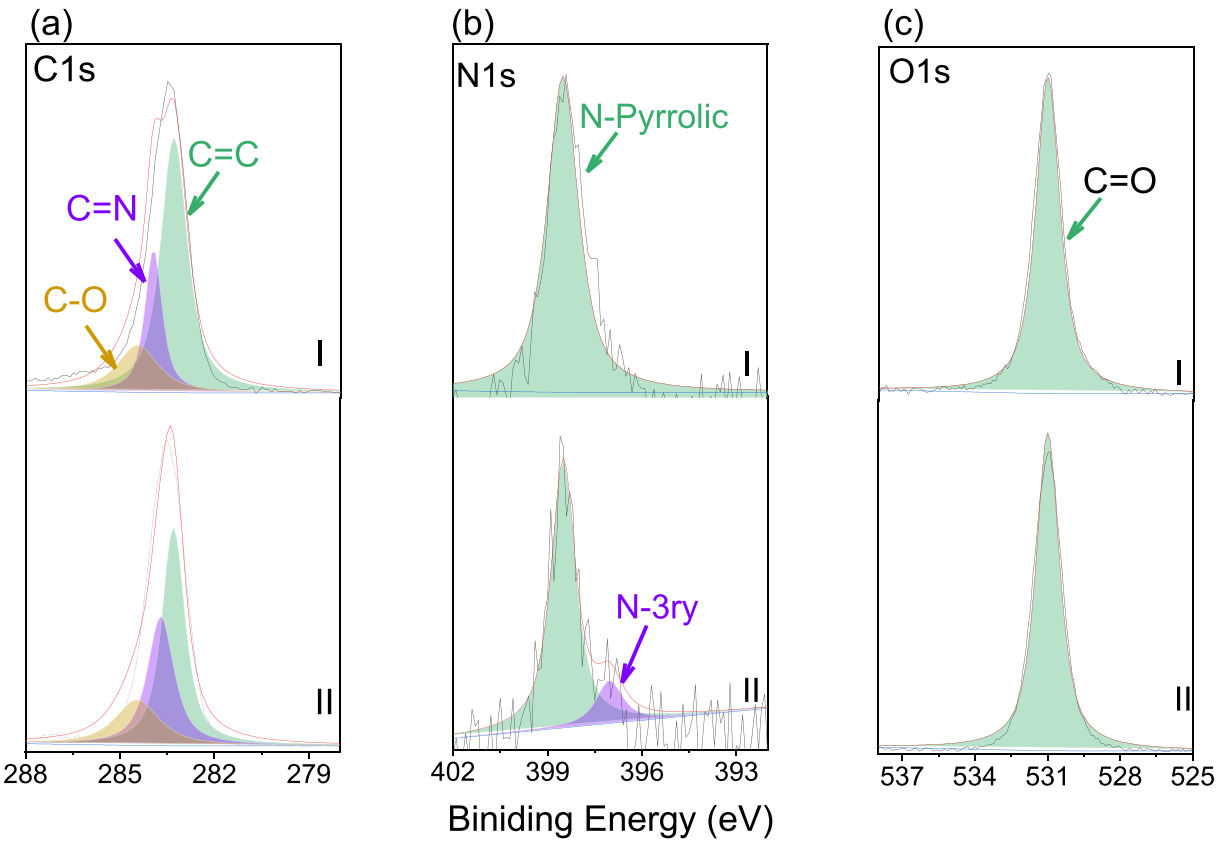

Fig. 2. High resolution XPS scans of (a) C, (b) N, and (c) O elements incorporated those Py-BD and TPA-BD CMPs. (I: Py-BD CMP and II: TPA-BD CMP).

nitrogen state in TPA-BD CMP, underscoring its significant role in the material's electrochemical features [52]. The O1s spectra of BD CMPs (Fig. 2c) revealed a single type of oxygen state located at 531.03 eV, which can be attributed to oxygen atoms double-bonded to carbon atoms (C=O). This suggests that the oxygen functionalities in both Py-BD and TPA-BD CMPs are primarily associated with carbonyl groups, which can influence the materials' chemical reactivity. Notably Table S1 summarizes the FWHMs and peak areas of the various chemical species detected in the XPS analysis of Py-BD and TPA-BD CMPs.

3.1.1. Physical features

The thermal stability of the CMPs, Py-BD and TPA-BD, was assessed using TGA under a nitrogenic environment. Basically, this analysis is crucial for understanding the thermal robustness of these materials, particularly in applications such as energy storage, where thermal stability can significantly impact performance and longevity. The TGA results indicated that the decomposition temperatures (T_{d10}) for Py-BD CMP and TPA-BD CMP were 434 °C and 385 °C, respectively. Actually, these values suggest that both materials exhibit considerable thermal stability (Fig. S1). The observed slightly higher T_{d10} of Py-BD CMP indicates that it can withstand elevated temperatures better than TPA-BD CMP before undergoing thermal degradation. As the Py subunits show higher planarity than TPA molecules therefore the Py-BD CMP can form physical stacking between its layers [53,54].

Further, the char yields at 800 °C were assessed, yielding values of 72.5 wt% for Py-BD CMP and 72.2 wt% for TPA-BD CMP (Fig. S1). Notably, the char yield represents the amount of residue remaining after complete thermal degradation, providing insight into the CMP's ability to retain structural integrity at elevated temperatures. As observed, those similar char yields for both CMPs suggest that they possess comparable thermal stability characteristics, with a substantial portion of the original material remaining after exposure to high temperatures. Moreover, the relatively high decomposition temperatures and char yields observed in both Py-BD and TPA-BD CMPs highlight their suitability for applications requiring thermal robustness [55]. Basically, the differences in decomposition temperatures between our BD CMPs may be attributed to their distinct chemical structures and compositions. The presence of different functional groups and the overall molecular architecture can influence thermal behavior, affecting how each CMP responds to heat. The higher T_{d10} for Py-BD CMP suggests a more thermally stable framework, potentially due to stronger intermolecular interactions or a more robust crosslinked structure compared to TPA-BD CMP. Again, the Py incorporated Py-BD CMP can form stacking in between its layers [56].

The porous properties of the synthesized BD-CMPs were evaluated using nitrogen adsorption–desorption assays at 77 K (Fig. S2). The isotherms of Py-BD and TPT-BD CMPs show a slight increase at low relative pressure, indicating that the materials are mainly microporous [57]. The BET surface areas (SBET) of Py-BD and TPA-BD CMPs were 250 and 87 $m^2 g^{-1}$, respectively (Table S2). The larger surface area of Py-BD CMP is attributed to the stronger π–π stacking of Py units compared to TPA units. At higher P/P_o, nitrogen uptake increases gradually, with hysteresis loops extending to low relative pressures, indicating a mix of type I and type IV isotherms and the presence of both micropores and mesopores [58]. NLDFT analysis of pore sizes and distributions shows that Py-BD and TPA-BD CMPs contain both micropores and mesopores of varying sizes.

The mesopore sizes of Py-BD CMP and TPA-BD CMP are dual, respectively 1.10 and 1.71 nm for the Py-BD CMP and 1.06 and 1.77 nm for TPA-BD CMP, these are formed either by elastic deformation of the pore structure or by swelling in liquid nitrogen. Similar results have been observed in other porous polymer-based irregular mesoporous structures. The total pore volumes (V_{total}) are 0.47 and 0.30 $cm^3 g^{-1}$ for Py-BD and TPA-BD CMPs, respectively. Motivated by their high surface areas and porous structures, BD-CMPs show promise as a new class of materials for supercapacitor electrodes [59]. Their inherent

microporosity is accessible to various targeted guest molecules such as electrolyte ions.

The morphologies of Py-BD and TPA-BD CMPs were examined using high-resolution transmission electron microscopy (HR-TEM). As shown in Fig. 3a and b, both CMPs consist of aggregated particles forming a continuous network, indicative of their highly cross-linked polymeric structures. The HR-TEM images reveal that the individual particles are predominantly spherical, with uniform size distribution, suggesting a controlled polymerization process. Such spherical aggregation is typical for CMPs and is consistent with their high surface areas and porosity. The observed particle morphology is expected to facilitate efficient ion transport and accessibility of the electrolyte within the porous framework, which is beneficial for electrochemical applications such as supercapacitors. The aggregated nature of the Py-BD and TPA-BD CMPs is further confirmed by field-emission scanning electron microscopy (FE-SEM) images (Fig. 3c and d). The SEM analysis reveals that both CMPs are composed of closely packed, spherical particles, consistent with the HR-TEM observations. The observed spherical morphology and particle aggregation indicate the formation of a continuous interconnected framework, which is typical of CMP materials. While SEM provides insight into the overall morphology, the porous nature and high surface area are confirmed by BET analysis.

3.1.2. Electrochemical performance

The electrochemical characterization of the newly synthesized Py-BD and TPA-BD CMPs was conducted using CV to evaluate their potential as electrode materials for supercapacitors. The experiments were performed within a potential window of 0 to −0.7 V versus Hg/HgO (Fig. 4a and b), utilizing a 1 M KOH electrolyte which is a common choice for supercapacitor applications due to its high ionic conductivity. The CV profiles of the Py-BD CMP exhibited a characteristic rectangular shape, indicative of its capacitive behavior, along with a distinct redox peak observed at approximately 0.55 V. This peak demonstrates the electrochemical activity associated with the redox processes occurring within the CMP matrix. Notably, the CV scans were carried out at varying potential rates from 5 to 200 mV s^{-1}, as well the persistence of the redox peak across these current densities suggests that the Py-BD CMP (Fig. 4a) maintains its electrochemical integrity and performance under different operational conditions. In contrast, the TPA-BD CMP (Fig. 4b) presented a smoother CV profile with a well-defined redox peak located around 0.3 V. This behavior indicates that while TPA-BD CMP also exhibits capacitive characteristics, its electrochemical response is markedly different from that of Py-BD CMP. The smoothness of the CV curve for TPA-BD CMP may suggest a more stable charge storage mechanism, potentially linked to its structural properties.

As we reported above, the surface area measurements revealed that Py-BD CMP possesses a surface area of 250 $m^2 g^{-1}$, significantly higher than that of TPA-BD CMP, which has a surface area of 87 $m^2 g^{-1}$. This disparity in surface area likely contributes to the differences in their electrochemical performance, as a larger surface area typically facilitates greater storage capacity.

Furthermore, the pore characteristics of both CMPs were analyzed. The Py-BD CMP exhibited pore widths of 1.10 nm and 1.71 nm, whereas TPA-BD CMP had slightly narrower pores at 1.06 nm and 1.77 nm. The pore volume measurements corroborate these findings, with Py-BD CMP showing a pore volume of 0.47 $cm^3 g^{-1}$ compared to TPA-BD's 0.06 $cm^3 g^{-1}$. These structural attributes are critical in determining the material's ability to facilitate ion transport during charge/discharge cycles. Interestingly, despite the superior surface area and pore volume of Py-BD CMP, the capacitance values indicate that TPA-BD CMP outperforms Py-BD CMP in terms of capacitance retention and overall electrochemical performance. This observation could be attributed to the intrinsic properties of TPA units in the TPA-BD CMP that enhance pseudocapacitance through redox-active sites. Actually, TPA is known for its strong electron-donating properties, which can facilitate interactions with cations such as K^+ [60–62]. The nitrogen atom in the TPA structure can act as a Lewis base, allowing it to coordinate with K^+ ions [63]. This interaction is further enhanced by the bulky nature of the TPA structure, which may create a favorable environment for ion binding due to steric effects [64]. The presence of multiple aromatic rings in TPA can also contribute to a suitable surface area for interaction, potentially increasing the binding affinity for K^+ ions. Moreover, TPA derivatives can form complexes with various cations and anions, indicating their ability to engage in supramolecular chemistry [65]. For instance, TPA has been reported to be effectively complex with fullerene derivatives, which suggests that its electron-rich nature allows for versatile interactions with positively charged species. This implies that TPA units could indeed interact more favorably with K^+ compared to Py units. On the other hand, pyrene is a polycyclic aromatic hydrocarbon that primarily exhibits hydrophobic characteristics and does not possess functional groups capable of strong Lewis acid-base interactions with K^+. While pyrene can participate in π-π stacking interactions due to its aromatic nature, it lacks the specific binding sites that facilitate coordination with cations. Consequently, the electrostatic interactions between pyrene and K^+ would be significantly weaker compared to those between TPA and K^+. However, the indirubin unit still plays an essential role by providing a conjugated backbone and additional redox-active carbonyl (C=O) functionalities, which contribute to charge delocalization and overall electrochemical activity. Therefore, the performance of these CMPs arises from a combined effect, where indirubin ensures structural conjugation and baseline redox activity, while the comonomer (particularly TPA) modulates and enhances the electrochemical response.

Electrochemical response of the Py-BD and TPA-BD CMPs was further investigated using GCD methodology across wide current densities between 1 and 20 A g^{-1} throughout a potential window of 0 to −0.7 V (Fig. 4c and d). The results revealed distinct characteristics in the discharge profiles of the two CMPs, providing insights into their electrochemical behavior. The discharge profile of the Py-BD CMP exhibited a triangular shape (Fig. 4c), which is typical for capacitive materials,

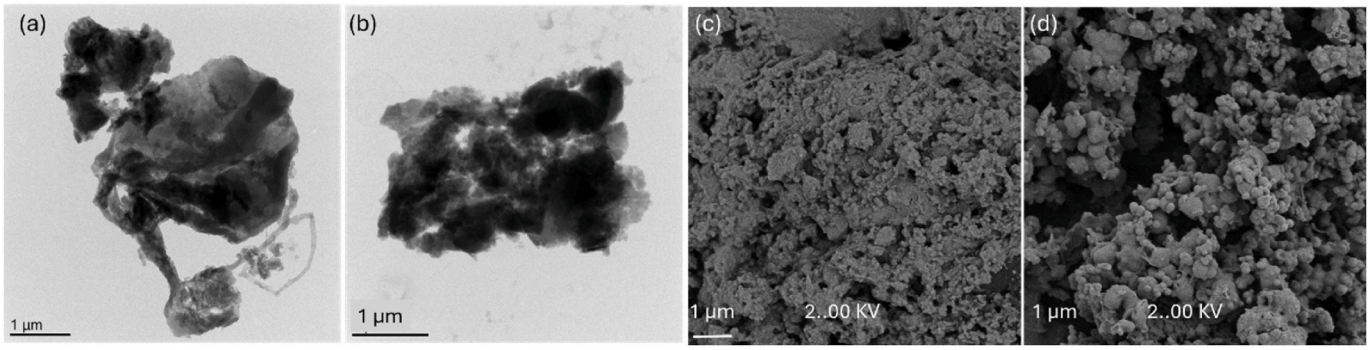

Fig. 3. (a, b) TEM of those Py-BD and TPA-BD CMPs respectively, (c, d) SEM of those Py-BD and TPA-BD CMPs respectively.

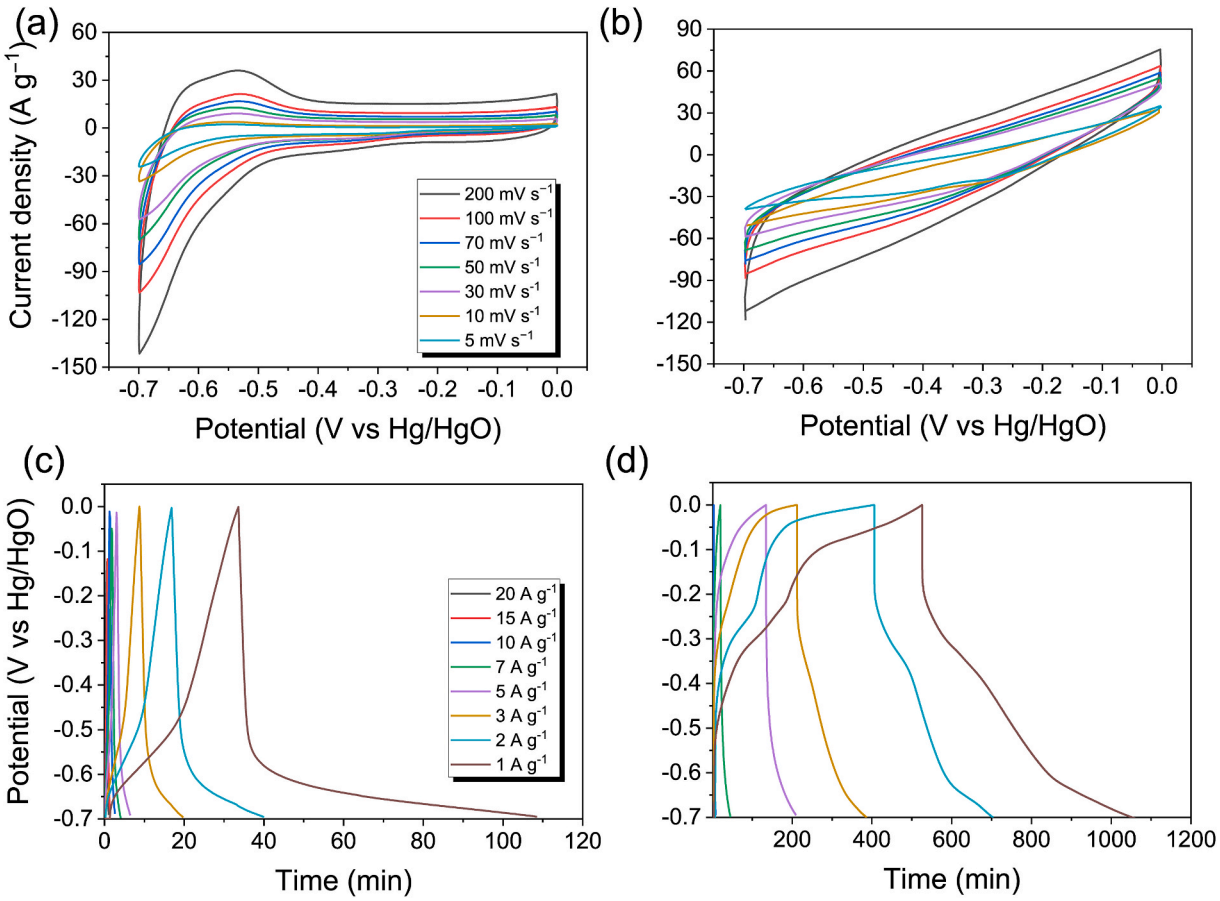

Fig. 4. CV sweeps at various scan rates of those (a) Py-BD and (b)TPA-BD CMPs. GCD scans of those (c) Py-BD and (d) TPA-BD CMPs under various current densities.

indicating a rapid charging storage mechanism. However, a significant internal resistance (IR drop) was noted during the discharge process, particularly at higher current densities. At a current density of 1 A g^{-1}, the discharge time recorded was 73 s. The pronounced IR drop suggests that while Py-BD CMP can facilitate charge storage effectively, it experiences considerable energy losses due to resistance within the material or at the electrode-electrolyte interface. In contrast, the TPA-BD CMP also demonstrated a triangular discharge profile but with a markedly reduced IR drop, indicative of improved conductivity and lower internal resistance. The discharge time for TPA-BD CMP at 1 A g^{-1} was significantly longer at 509 s. This extended discharge time reflects not only better charge retention but also enhanced kinetics associated with the electrochemical processes occurring within the polymer matrix. The observed severe bent in the triangular shape of the TPA-BD CMP discharge curve may be attributed to redox effects occurring during the charge/discharge cycles. The presence of redox-active TPA units in TPA-BD CMP facilitates additional charge storage mechanisms beyond simple electric double-layer capacitance (EDLC), allowing for more complex electron transfer processes. This redox activity can contribute to an increase in capacitance as well as prolonging discharge times by enabling more extensive ion intercalation and deintercalation processes. The differences in discharge behavior between Py-BD and TPA-BD CMPs can be explained by their structural and electronic properties. The TPA units in the TPA-BD CMP not only enhance conductivity through better electron transport but also promote effective interactions with K^+ ions in the electrolyte due to their favorable coordination chemistry. This interaction is likely responsible for the reduced IR drop and extended discharge times observed for the TPA-BD CMP (Fig. 4c) compared to the Py-BD CMP (Fig. 4d). The absence of distinct redox peaks in the CV curves of TPA-BD CMP may be attributed to the fast and highly reversible surface redox reactions, which can appear as quasi-rectangular CV shapes rather than well-defined peaks. In contrast, the GCD curves show slight deviations from ideal triangular plateaus, indicating the presence of pseudocapacitive contributions. This behavior is commonly observed in porous polymer-based electrodes, where electric double-layer capacitance and fast surface redox reactions coexist. The specific capacitances of Py-BD and TPA-BD CMPs were calculated using the GCD methodology, employing equation (1), C_p considers the specific capacitance (F g^{-1}), I_m consider the discharge current (A), Δt assumes the discharge time (s), m assumes the mass of the active material (g), and ΔV is the potential window (V). As expected above, the TPA-BD CMP exhibited remarkably higher capacitance values across all current densities tested (Fig. 5a) (916.55 F g^{-1} at 1 A g^{-1}), reflecting its superior charge storage capabilities compared to the Py-BD CMP which recorded a 107.64 F g^{-1} at 1 A g^{-1}.

The electrochemical active surface area (ECSA) was estimated from the double-layer capacitance (Cdl), obtained from cyclic voltammetry in the non-Faradaic region at scan rates ranging between 30 and 100 mV s^{-1}. Using a commonly accepted specific capacitance value of 40 μF cm^{-2} for carbon-based materials in aqueous electrolytes, the calculated ECSA values were 64.5 cm^2 for Py-BD CMP and 6.75 cm^2 for TPA-BD CMP. Although Py-BD CMP exhibits a significantly larger accessible electrochemical surface area, the higher specific capacitance observed for TPA-BD CMP suggests that pseudocapacitive redox contributions play a dominant role in its charge storage mechanism. This indicates that capacitance in these CMP systems is governed not only by surface area but also by the intrinsic electrochemical activity of the functional groups within the polymer framework.

The higher specific capacitance of the TPA-BD CMP can be explained by the presence of redox-active TPA units, which facilitate additional charge storage mechanisms beyond conventional EDLC. This pseudocapacitance contributes to a greater overall capacitance, particularly at

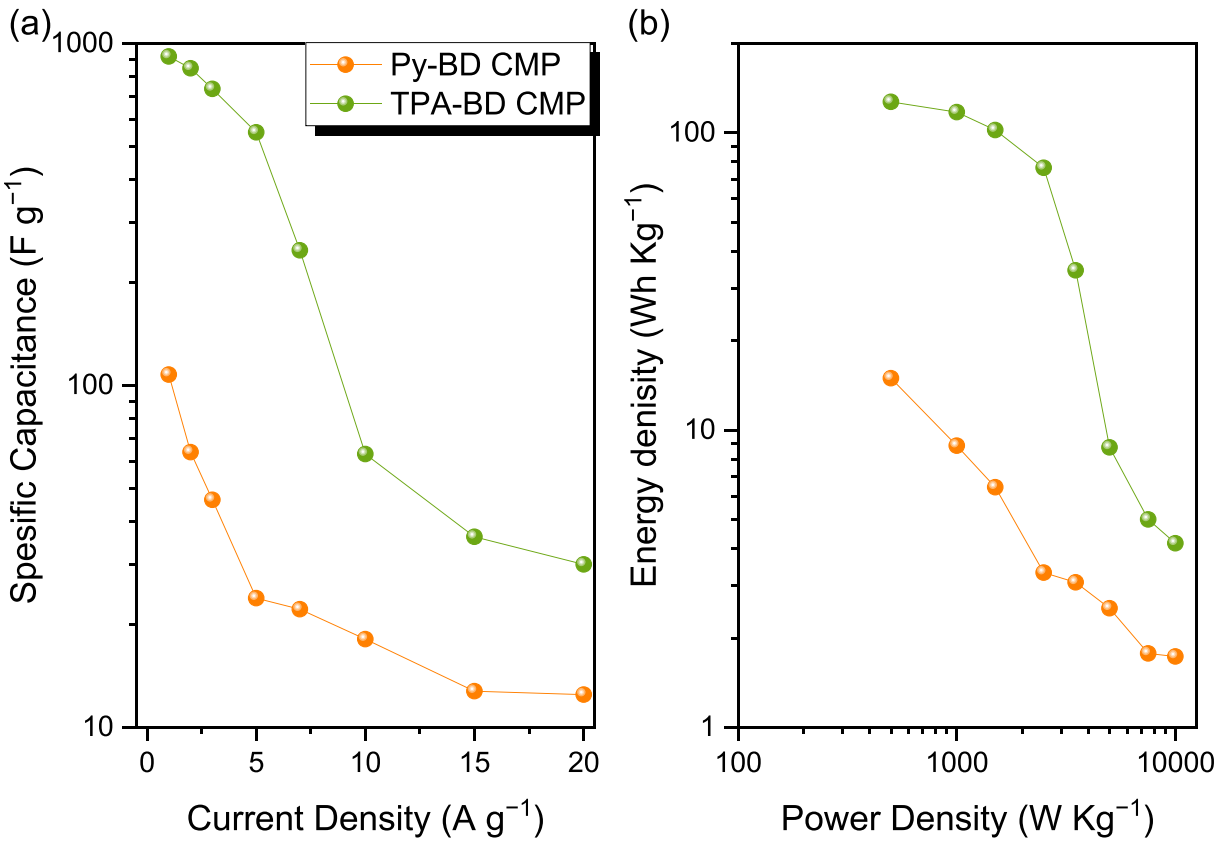

Fig. 5. (a) Specific capacitance correlated current densities and (b) Ragone plots of those Py-BD and TPA-BD CMPs.

lower current densities where ion diffusion and intercalation processes are more favorable. In contrast, the Py-BD CMP's specific capacitance values decline more sharply with increasing current density (Fig. 5a), indicating that it may be limited by slower ion transport kinetics and higher internal resistance, as evidenced by the significant IR drop observed during galvanostatic discharge tests. The triangular discharge profile of Py-BD CMP further suggests capacitive behavior but reveals limitations in maintaining performance at elevated current densities. Specific capacitances of BD CMPs show better performance than those reported previously (Table S2). The densities of energy as well as power of those CMPs, Py-BD and TPA-BD (Fig. 5b) were estimated using the following equations (2) and (3), where E_g is the energy density (Wh kg^{-1}), C_p is the specific capacitance (F g^{-1}), ΔV is the potential window (V), and Δt is the discharge time (s). The analysis reveals a clear distinction in the performance characteristics of Py-BD and TPA-BD CMPs regarding densities of energy and power. For Py-BD CMP, there is a noticeable decrease in energy density as power density increases, which is indicative of a typical trade-off between energy and power in supercapacitor electrode materials. At lower power densities, such as at 500 W kg^{-1}, Py-BD CMP achieves an energy density of approximately 14.95 Wh kg^{-1}, but this value declines sharply with increasing power demands, reaching only about 1.73 Wh kg^{-1} at a power density of 10,000 W kg^{-1}. This trend suggests that while Py-BD CMP can deliver moderate energy storage capabilities, its performance diminishes significantly under high power conditions, likely due to limitations in ion transport kinetics and increased internal resistance. In contrast, the TPA-BD CMP demonstrates exceptional energy density values across all tested power densities, starting at an impressive 127.30 Wh kg^{-1} at a power density of 500 W kg^{-1} and maintaining substantial energy storage capabilities even at higher power densities, with an energy density of approximately 4.16 Wh kg^{-1} at a power density of 10,000 W kg^{-1}. Overall, those energy and power densities of BD CMPs show comparable behaviours than those reported previously (Table S3). This remarkable performance can be attributed to the redox-active nature of the TPA units in TPA-BD CMP, which not only enhances charge storage through pseudocapacitance but also facilitates efficient charge/discharge kinetics. The data indicate that TPA-BD CMP offers a superior balance between energy and power densities compared to Py-BD CMP, rendering it a more suitable candidate in instruments requiring both high energy storage capacity and rapid discharge capabilities. The cycling stability and performance of Py-BD and TPA-BD CMPs (Fig. S3a) were evaluated through GCD tests conducted at a current density of 10 A g^{-1} over 10,000 cycles. The results demonstrated significant differences in both capacitance retention and overall cycling efficiency between the two materials.

At the completion of 10,000 cycles, the specific capacitance for Py-BD CMP was measured at 16.45 F g^{-1}, while the TPA-BD CMP displayed a notably capacitance of 54.44 F g^{-1} at a current density of 10 A g^{-1}(Fig. S3a–b). This stark contrast in capacitance values indicates that TPA-BD CMP not only retains a greater amount of charge storage capability but also suggests superior electrochemical stability throughout the cycling process. In terms of cycling stability, Py-BD CMP maintained an impressive 90.80% of its initial capacitance after 10,000 cycles, demonstrating robust performance under prolonged cycling conditions. Conversely, the TPA-BD CMP displayed a slightly lower retention rate of 86.40%. Although both materials exhibited high cycling stability, the raised absolute capacitance retention in TPA-BD CMP signifies its enhanced ability to withstand repeated charge-discharge cycles while maintaining effective energy storage. The superior performance of the TPA-BD CMP can be attributed to several factors related to its molecular structure and electrochemical properties. Further, the tunability between TPA and BD subunits. The presence of redox-active TPA units within TPA-BD CMP enhances its electrochemical activity, allowing for more efficient charge storage mechanisms beyond simple EDLC as we already explained above. This redox activity contributes to the overall capacitance and enables better

retention during cycling, as it facilitates reversible faradaic reactions that can replenish charge more effectively than purely capacitive processes. In contrast, while Py-BD CMP demonstrates commendable cycling stability with a high percentage retention, its lower specific capacitance at cycle 10,000 indicates limitations in its charge storage capabilities over extended use. The observed decline in capacitance could be due to factors such as increased internal resistance or structural degradation during cycling, which may hinder ion transport and reduce overall electrochemical performance. These results highlight the interest of material design in optimizing supercapacitor performance. The enhanced cycling stability and higher specific capacitance retention observed in TPA-BD CMP position as a more favorable candidate for devices requiring long-lasting energy storage solutions.

XPS analysis indicates that the overall chemical structure of the CMP framework remains stable after cycling. A slightly higher percentage of C1s signal was observed in the post-cycling electrode, which can reasonably be attributed to the presence of conductive carbon black used in the electrode slurry formulation. Since XPS is a surface-sensitive technique, the contribution from carbon black on the electrode surface can increase the relative carbon signal without indicating degradation of the CMP framework (Fig. S4a–b). Further, The TEM images confirm that the spherical morphology remains well preserved after 10,000 cycling. Interestingly, the spherical features appear more clearly defined after repeated charge–discharge processes, which may be attributed to improved electrolyte penetration and removal of loosely attached surface species during cycling. Importantly, no structural collapse or morphological degradation was observed (Fig. S4c–d).

The capacitive contributions to the total charge storage capacity of the Py-BD and TPA-BD CMPs (Fig. 6a and b) were analyzed using the equations: $i(v) = k_1 v + k_2 v^{1/2}$ or $i(v)/v^{1/2} = k_1 v^{1/2} + k_2$, where $i(v)$ considers the current response, v considers the scan rate, k_1 displays the capacitive inclusion, and k_2 corresponds to the diffusion-controlled inclusion. This provides insights into the mechanisms governing charge storage within these materials. At a scan rate of 5 mV s^{-1}, the capacitive and diffusion contributions for Py-BD CMP were determined to be 90.59% and 9.41%, respectively (Fig. 6c). In contrast, TPA-BD CMP exhibited a lower capacitive contribution of 72.43% and a higher diffusion contribution of 27.56% (Fig. 6d). The differences in capacitive and diffusion-controlled contributions are indeed related to structural factors such as pore architecture, BET surface area, and intrinsic redox activity. The Py-BD CMP, with its higher surface area, shows more dominant surface-controlled (capacitive) behavior. In contrast, TPA-BD CMP exhibits a mixed contribution, where diffusion-controlled processes are more noticeable compared with the Py-BD CMP due to its denser framework and stronger redox-active sites.

The data indicate that the Py-BD CMP demonstrates a strong capacitive behavior across all scan rates, with contributions exceeding 90% even at higher rates, reflecting its efficient charge storage capability primarily through EDLC mechanisms. This behavior is indicative of rapid ions adsorption and desorption processes at the electrode interface, which are essential for high-rate performance in super-

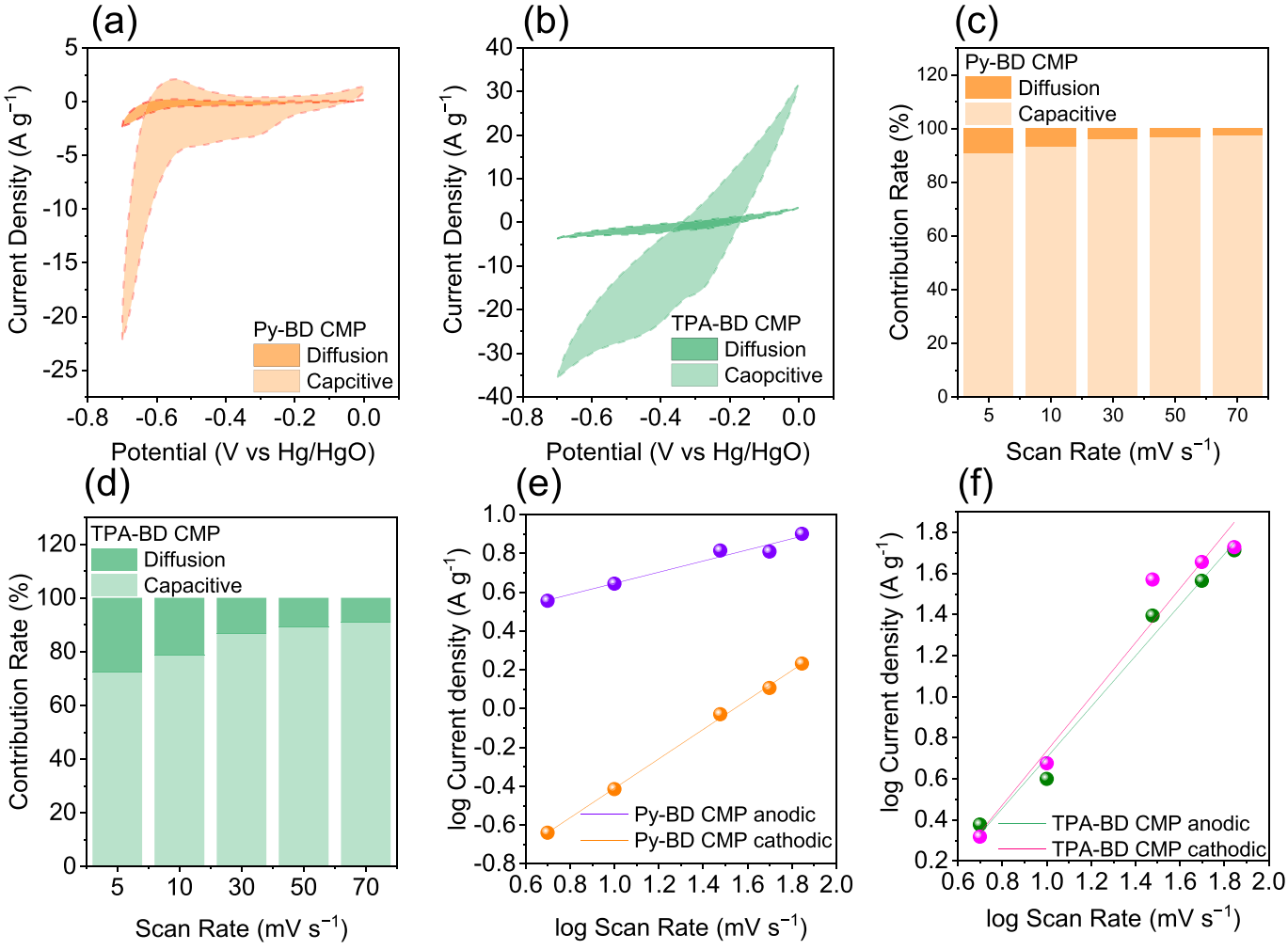

Fig. 6. (a, b) The CV integration of those capacitive as well as diffusion at 5 mV s−^{1}, (c, d) the inclusion percentages of them within wide scan ranges and (e, f) log/log correlation of the current and scan rates of both anodic and cathodic currents of those Py-BD (a, c, e) and TPA-BD (b, d, f) CMPs respectively.

capacitors. Conversely, the TPA-BD CMP shows a significant increase in diffusion-controlled contributions as the scan rate increases, particularly at lower rates where it reaches 27.56% at 5 mV s^{-1} and decreases to 9.23% at elevated rates (70 mV s^{-1}). This suggests that while TPA-BD CMP can also facilitate rapid charge storage through capacitive mechanisms, it relies more on ion diffusion processes within its structure, which may limit its performance at very high scan rates compared to Py-BD CMP. The differences in performance can be attributed to the structural characteristics of each CMP; TPA-BD CMP's redox-active TPA units may introduce additional pathways for charge storage but also complicate ion transport dynamics compared to the more straightforward capacitive mechanism observed in the Py-BD CMP. To assess the capacitive behavior of the Py-BD and TPA-BD CMPs, we employed a power law to analyze the relationship in-between current density i as well as scan rate (v). The relationship was expressed as: $i = a \cdot v^b$ whereas a and b are constants. By taking the logarithm of both sides, we can derive $\log(i) = \log(a) + b \cdot \log(v)$. This equation allows us to plot $log\, i$ against $log\ (v)$ (Fig. 6e and f), where the slope of the resulting line corresponds to the value of b. The magnitude of b provides insights into the dominant charge storage mechanism within the CMPs. For Py-BD CMP (Fig. 6e), the slope obtained from the log-log plot was 0.28, while for TPA-BD CMP, the slope was significantly higher at 1.3 (Fig. 6f). These values suggest distinct mechanisms governing charge storage in each material. Regarding the Py-BD CMP ($b = 0.28$) indicates that the current response is less sensitive to changes in scan rate, suggesting that a substantial portion of charge storage occurs through capacitive mechanisms. The value being less than 0.5 implies that diffusion processes play a minimal role in charge transport at lower scan rates, highlighting that Py-BD CMP primarily relies on surface capacitance for energy storage. Further, this behavior is consistent with the high capacitive contribution observed earlier, where approximately 90.59% of charge storage was attributed to capacitive mechanisms under scan rate of 5 mV s^{-1}. In contrast, the b value of 1.3 for TPA-BD CMP (Fig. 6f) indicates a strong dependence of current on scan rate, suggesting that diffusion-controlled processes significantly influence charge storage. This value being greater than 1 implies that TPA-BD CMP exhibits a higher degree of pseudocapacitance, likely due to redox reactions associated with the TPA units. The higher reliance on diffusion processes aligns with earlier findings where TPA-BD CMP showed lower capacitive contributions at higher scan rates, indicating that ion transport within the TPA-BD CMP matrix may limit performance under rapid cycling conditions.

To further elucidate the electrochemical response of the Py-BD and TPA-BD CMPs, we conducted EIS measurements. The resulting Nyquist plots (Fig. S5a) were fitted using the equivalent circuit shown in Fig. S5b, comprising the bulk solution resistance (R_s), charge transfer resistance (R_{ct}), and a constant phase element (CPE) accounting for the non-ideal capacitive behavior of the porous electrode surface.

The Nyquist plots for both materials display a small semicircle in the high-frequency region, followed by a steep linear portion in the low-frequency region. The high-frequency semicircle is attributed to the R_{ct} at the electrode/electrolyte interface. For the Py-BD CMP, the R_{ct}value was notably lower than that of TPA-BD CMP. This suggests that the Py-BD CMP possesses a more favorable electronic structure or higher wettability, facilitating faster faradaic charge transfer, likely stemming from its redox-active pyrene units which enhance interfacial kinetics. The low R_{ct} values for both materials confirm their good electrochemical reactivity and low energy dissipation during charge storage.

The intercept of the semicircle with the real axis (Z') at the highest frequency corresponds to the bulk R_s. The R_s values were 26.6 Ω for Py-BD and 27.7 Ω for TPA-BD, indicating consistent electrolyte conductivity and electrode preparation across samples. The subsequent vertical line in the low-frequency zone, nearly parallel to the imaginary axis ($-Z''$), signifies ideal capacitive behavior and confirms efficient electrolyte ion diffusion into the microporous network of the CMPs. The slightly more vertical slope observed for the Py-BD CMP implies a lower diffusion resistance compared to TPA-BD, which may be attributed to a more open pore architecture facilitating ion mobility.

To quantify the frequency response, Bode phase angle and magnitude plots were analyzed (Fig. S5c). In the low-frequency region of the Bode magnitude plot, a linear negative slope confirms the dominance of capacitive behavior, as the impedance is inversely proportional to frequency.

A critical parameter derived from the Bode plot is the characteristic relaxation time constant (τ_0), which represents the minimum time needed to discharge all the energy with an efficiency greater than 50%. This is calculated from the knee frequency (f_0) at which the phase angle reaches −45° ($\tau_0 = 1/f_0$). The knee frequency for the Py-BD CMP was 340.56 Hz, corresponding to a very fast time constant of 2.94 ms (Fig. S5d). In contrast, TPA-BD CMP exhibited a knee frequency of 2.19 Hz, resulting in a significantly slower time constant of 456 ms (Fig. S5d). The superior rate capability of Py-BD CMP is evidenced by its higher knee frequency, indicating that it can maintain capacitive behavior even under rapid charge/discharge cycles. This is likely due to the planar, rigid structure of Py promoting better π-π stacking and a more interconnected conductive network within the polymer matrix, facilitating faster electron transport. The lower knee frequency for TPA-BD CMP suggests that while its TPA core contributes substantial pseudocapacitance (enhancing energy density), the bulkier structure may impede ion kinetics at high frequencies, making it more suitable for applications prioritizing energy storage over high power delivery.

3.1.3. Two electrode device system (coin cell)

In the construction of a symmetric supercapacitor, the TPA-BD CMP was employed as both the cathode as well as anode, demonstrating its versatility as an electrode material. The preparation involved creating a suspension of the CMP according to the specified proportions, which was subsequently applied to carbon paper to form the electrode. An aqueous electrolyte solution of 1.0 M KOH was utilized in conjunction with a Selemion AMV membrane to facilitate ion transport between the electrodes during operation. Electrochemical characterization was performed using CV across a range of scan rates in-between 5 to 200 mV s^{-1} and within a potential window of −0.3 to 0.5 V (Fig. 7a). The resulting CV curves, as illustrated in the accompanying figures, exhibited a distinctly rectangular shape, characteristic of ideal supercapacitor behavior. This rectangular profile is indicative of the combined contributions from EDLC and pseudocapacitance associated with the electroactive components of TPA-BD CMP. Notably, this rectangular shape was consistently maintained across the various scan rates tested, highlighting the stability and reliability of the electrochemical performance of the symmetric supercapacitor configuration. The preservation of this rectangular form under differing scan rates suggests superior charge storage and rapid ion movement capabilities within the TPA-BD CMP electrodes, reinforcing their suitability for high-performance energy storage utilizations. This behavior assures the prospecting of TPA-BD CMP in advanced supercapacitor designs, where both energy density and power density are critical for practical applications.

The GCD profiles were conducted on coin cells incorporating the TPA-BD CMP as the electrode material, across a range of current densities ranging between 1 and 20 A g^{-1} (Fig. 7b). The resulting discharge profiles exhibited a characteristic triangular shape, indicative of the capacitive behavior of the supercapacitor. At a current density of 1 A g^{-1}, the GCD plateau demonstrated a significantly longer discharge time compared to higher current densities. This extended discharge time reflects the enhanced charge storage capacity and energy retention of the TPA-BD CMP at lower current densities, allowing for more complete ion intercalation and deintercalation processes. The triangular shape of the discharge profile confirms the efficient charge storage mechanism facilitated by both EDLC and pseudocapacitance associated with the redox-active components in the TPA-BD CMP. As the current density raised, a corresponding reduction in discharge time was observed, which is typical for supercapacitors due to reduced ions transport times at

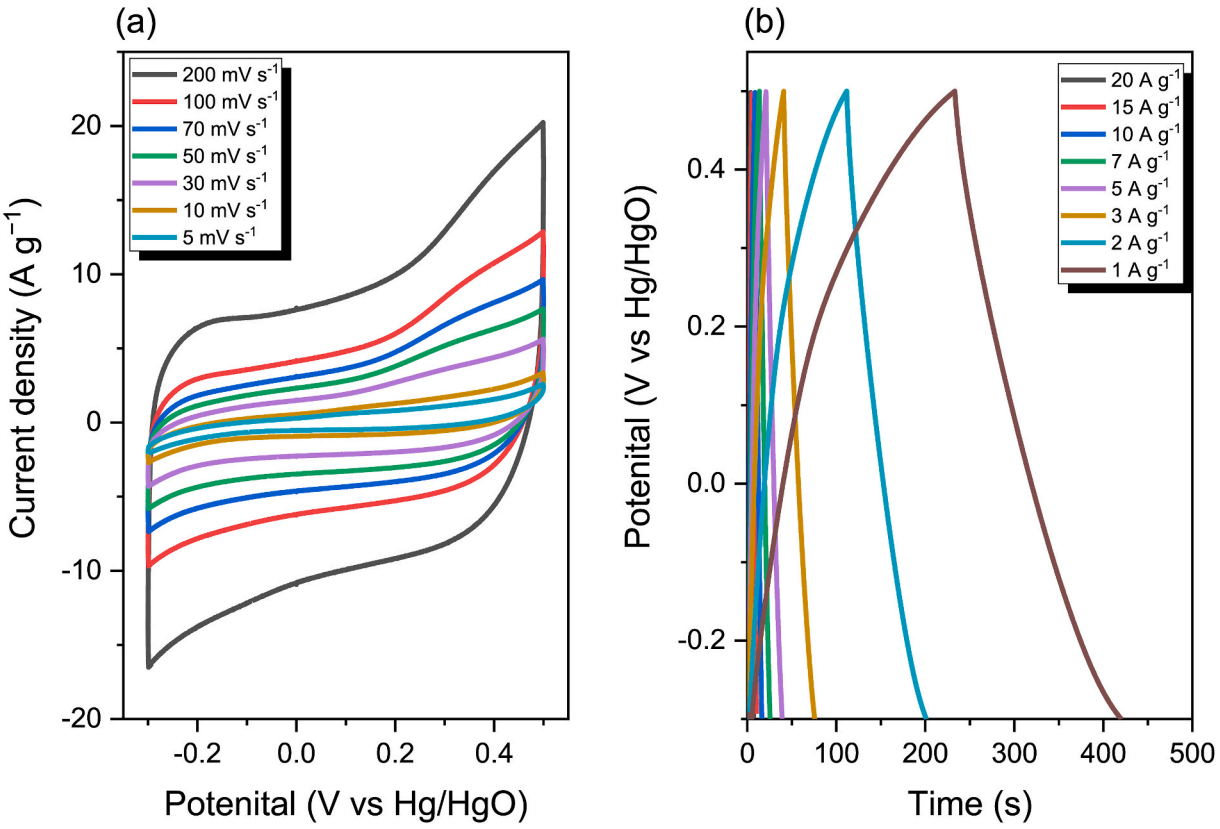

Fig. 7. CV and GCD sweep scans of coin cell incorporated TPA-BD CMP electrode.

higher rates (Fig. S6a). The TPA-BD CMP incorporated coin cell shows a specific capacitance of 232.5 F g^{-1} at 1 A g^{-1} (Table S4). However, the persistence of the triangular shape across varying current densities indicates that TPA-BD CMP maintains its capacitive characteristics even under rapid cycling conditions. The capacitance of the device incorporating the TPA-BD CMP was determined from the GCD plateaus at many current densities. These statistical indicate a gradual decline in specific capacitance with raising current density, which is typical for supercapacitor materials. The high specific capacitance observed under reduced current densities reflects the effective charge storage capabilities of the TPA-BD CMP, attributed to its favorable structural and electrochemical properties. As the current density increases, the reduction in specific capacitance suggests that ion transport limitations begin to affect performance, highlighting the trade-off between power and energy density in supercapacitor applications. The power and energy densities regarding the coin cell incorporating the TPA-BD CMP were evaluated based on the results obtained from the GCD curves. Under a power density of 500 W kg^{-1}, the energy density was measured at approximately 32.29 Wh kg^{-1} (Fig. S6b), comparable versus those earlier reported materials (Table S4), demonstrating the material's capability for effective energy storage. As the power density increased, a corresponding decrease in energy density was observed, which is a common trend in supercapacitor performance. This relationship highlights the inherent trade-off between energy and power densities, where higher power demands typically result in reduced energy retention. Despite this decline, the TPA-BD CMP maintained competitive energy density values across a range of power densities, underscoring its prospection as an efficient electrode moiety for supercapacitor applications. The ability of TPA-BD CMP to deliver substantial energy density at relatively high power densities emphasize its suitability for applications requiring both rapid discharge capabilities and significant energy storage. These findings suggest that TPA-BD CMP can effectively balance the dual requirements of energy and power, making it an ideal candidate for advanced energy storage systems where performance and efficiency are critical.

To further investigate the electrochemical behaviour of TPA-BD CMP, we examined the correlation between the $(\nu^{1/2})$ and $\left(i/\nu^{1/2}\right)$ (Fig. S7a). The data revealed a correlation that allowed us to assess the inclusions of capacitive as well as diffusion-controlled processes to the overall charge storage mechanism. At a scan rate of 5 mV s^{-1}, the percentage contributions were detected to be approximately 56.54% for capacitive behaviour and 43.35% for diffusion-controlled capacitance (Fig. S7b). This indicates that a significant portion of charge storage in the TPA-BD CMP is attributed to capacitive mechanisms, which is favorable for high-rate performance in supercapacitor applications. We also analyzed the relationship between varying scan rates and their corresponding capacitive and diffusion percentages. The results demonstrated that as the scan rate increased, the capacitive contribution generally increased while the diffusion-controlled contribution decreased. For instance, at a scan rate of 5 mV s^{-1}, the capacitive contribution was 56.65%, which increased to 83.02% at 70 mV s^{-1} (Fig. S7c), illustrating a shift toward faster charge storage mechanisms at higher rates. Conversely, the diffusion contribution reduced from 43.35% at 5 mV s^{-1} to 16.98% at 70 mV s^{-1}, highlighting the reduced influence of ion diffusion under rapid cycling conditions. Notably, the charge storage behaviour of TPA-BD CMP shows consistent trends across both three-electrode and coin cell configurations. In the three-electrode system, the material exhibits a combination of capacitive and diffusion-controlled processes, reflecting its intrinsic electrochemical characteristics. In the coin cell device, a similar mechanism is observed; however, the capacitive contribution becomes more dominant with increasing scan rate (from ~56.6% at 5 mV s^{-1} to ~83.0% at 70 mV s^{-1}), indicating that fast surface-controlled processes govern charge storage under practical operating conditions, while diffusion effects are more pronounced at lower scan rates. This consistency confirms that TPA-BD

CMP maintains efficient and adaptable charge storage behaviour from fundamental evaluation to device-level application. To quantify these relationships further, we employed a power law equation to analyze the correlation between *i* and *v*. By plotting log (*i*) against log (*v*) (Fig. S7d), we were able to derive a slope of 1.59. This slope indicates that the current response is significantly influenced by the scan rate, suggesting a strong dependence on both capacitive and diffusion-controlled processes within the TPA-BD CMP. A slope greater than 1 implies that as the scan rate increases, there is an enhanced capacity for charge storage due to pseudocapacitance mechanisms associated with the redox-active components of the TPA-BD CMP.

To evaluate the electrochemical kinetics and charge storage behaviour of the TPA-BD CMP electrode in a practical two-electrode configuration, EIS was performed on the assembled coin cell. The resulting Nyquist plot (Fig. S8a) was analyzed using the equivalent circuit model depicted in Fig. S7b.

The Nyquist plot exhibits a small, depressed semicircle in the high-frequency region, followed by an almost vertical line in the low-frequency region. The intercept of the semicircle with the real axis (Z′) at the highest frequency corresponds to the equivalent R_s, measured to be 4.42 Ω. This R_s value encapsulates the total ohmic resistance of the system, including the intrinsic resistance of the current collectors, the bulk resistance of the CMP material, and the ionic resistance of the electrolyte within the separator and electrode pores. The relatively low R_s value indicates good electronic conductivity of the TPA-BD CMP electrode and effective wetting by the electrolyte, ensuring minimal ohmic losses during charge/discharge processes.

The diameter of the high-frequency semicircle represents the R_{ct}, which is associated with the faradaic processes and ionic transport at the electrode/electrolyte interface. The relatively small diameter observed for TPA-BD CMP suggests that the TPA-based CMP network facilitates efficient charge transfer kinetics. This can be attributed to the redox-active nature of the TPA core, which undergoes reversible oxidation, lowering the energy barrier for interfacial charge transfer.

In the low-frequency region, the nearly vertical line is characteristic of ideal capacitive behaviour. This confirms that the charge storage is predominantly governed by a surface-controlled process with rapid ion diffusion into the microporous framework. The steep slope indicates low diffusion resistance (Warburg impedance) within the CMP's pore channels, signifying that the electrolyte ions can readily access the electroactive sites throughout the polymer network.

The Bode magnitude plot (Fig. S8c) further supports these findings. The impedance ([Z]) is high at low frequencies and decreases with increasing frequency, demonstrating a transition from capacitor-dominated behaviour to resistor-dominated behaviour. The slope of this transition is indicative of the material's response time.

The frequency-dependent Bode phase-angle plot (Fig. S8d) provides a quantitative measure of this transition. At f_0, the resistive and capacitive components of the impedance are equal. For the TPA-BD CMP electrode, the knee frequency was determined to be 65.82 Hz.

This knee frequency corresponds to a relaxation time constant ($\tau_0 = 1/f_0$) of approximately 15.2 ms. The time constant represents the minimum time required to discharge all the stored energy with an efficiency greater than 50%. A τ_0 of 15.2 ms is a highly competitive value, indicating that the TPA-BD CMP electrode possesses excellent rate capability and can deliver its stored energy effectively under rapid charge/discharge conditions.

The stability of the TPA-BD CMP electrode incorporated in the coin cell was evaluated through coulombic efficiency measurements, which yielded a value of 78.52 F g^{-1} at 10 A g^{-1} after 5000 cycles out of 93.70 F g^{-1} at 10 A g^{-1} though the first cycle (Fig. S9a). This metric reflects the effective charge-discharge performance of the electrode material over multiple cycles, indicating its ability to retain a substantial amount of charge during operation. Additionally, the coin cell demonstrated an impressive capacity retention of 79.37% of its initial capacity after 10,000 cycles (Fig. S9b). While the retention value is moderate compared to some reported systems, it remains comparable to several previously reported porous polymer-based supercapacitors, as summarized in comparison Table S4. On the other hand, this level of capacity retention underscores the robustness and durability of the TPA-BD CMP electrode, suggesting that it can maintain efficient energy storage capabilities over time. The combination of high coulombic efficiency and significant capacity retention highlights the potential of the TPA-BD CMP as a reliable electrode material for supercapacitor applications, where long-term stability and performance are critical for practical use. These findings affirm the suitability of the TPA-BD CMP for advanced energy storage systems, providing confidence in its performance under real-world operating conditions. Future work will focus on practical device demonstrations, such as powering LEDs or small electronic devices, to further validate the real-world applicability of these materials.

4. Conclusion

This work demonstrated the successful design and analysis of two CMPs, Py-BD and TPA-BD CMPs, incorporating indirubin-based units. The TPA-BD CMP exhibited superior properties, including an enhanced thermal stability, and a higher specific capacitance compared to the Py-BD CMP. The electrochemical evaluation of the TPA-BD CMP in a two-electrode coin cell system revealed high capacitance and stability, underscoring its power as an advanced electrode for supercapacitors. The integration of indirubin derivatives into CMP structures leveraged their redox activity to enhance pseudocapacitance, contributing to improved energy storage capacity. The findings of this research highlight the importance of molecular design in enhancing the performance of CMPs for energy storage apparatus. By exploring the structural and electrochemical properties of these materials, we provided insights into the role of indirubin-based CMPs in advancing supercapacitor technology. Future studies can build upon these results by further optimizing the chemical inclusions as well as structural properties of CMPs to facilitate their energy density and power density. Additionally, exploring the scalability and practical implementation of these materials in real-world energy storage systems will be crucial for their widespread adoption.

CRediT authorship contribution statement

Mohammed G. Kotp: Conceptualization, Data curation, Formal analysis, Validation, Visualization, Writing – original draft, Writing – review & editing. **Shiao-Wei Kuo:** Funding acquisition, Resources, Supervision, Writing – review & editing.

Declaration of competing interest

The authors declare that they have no known competing financial interests or personal relationships that could have appeared to influence the work reported in this paper.

Appendix A. Supplementary data

Supplementary data to this article can be found online at https://doi.org/10.1016/j.jpowsour.2026.240417.

Data availability

The data that has been used is confidential.

References

[1] S.V. Bhosale, S.V. Bhosale, Advancement in supercapacitors: breaking barriers and shaping into amazing applications, Chem. Sci. 16 (2025) 10159–10227, https://doi.org/10.1039/D5SC01955A.
[2] T. Li, Y.-F. Wang, Z. Yin, J. Li, X. Peng, M.-H. Zeng, The sequential structural transformation of a heptanuclear zinc cluster towards hierarchical porous carbon

for supercapacitor applications, Chem. Sci. 13 (2022) 10786–10791, https://doi.org/10.1039/D2SC03987G.
[3] Z. Abdin, Shaping the stationary energy storage landscape with reversible fuel cells, J. Energy Storage 86 (2024) 111354, https://doi.org/10.1016/j.est.2024.111354.
[4] H. Jafarizadeh, E. Yamini, S.M. Zolfaghari, F. Esmaeilion, M.E.H. Assad, M. Soltani, Navigating challenges in large-scale renewable energy storage: barriers, solutions, and innovations, Energy Rep. 12 (2024) 2179–2192, https://doi.org/10.1016/j.egyr.2024.08.019.
[5] M.K. Khan, M. Raza, M. Shahbaz, U. Farooq, M.U. Akram, Recent advancement in energy storage technologies and their applications, J. Energy Storage 92 (2024) 112112, https://doi.org/10.1016/j.est.2024.112112.
[6] M.G. Kotp, A.F.M. El-Mahdy, M.M. Chou, S.-W. Kuo, Electronic nature of linkers based conjugated microporous polymers: a sustainable approach to enhance CO2 capture, New J. Chem. 48 (2024) 14435–14443, https://doi.org/10.1039/D4NJ02404D.
[7] M.G. Kotp, S.-W. Kuo, Harnessing solar energy with porous organic polymers: advancements, challenges, economic, environmental impacts and future prospects in sustainable photocatalysis,, Mater. Today Chem. 41 (2024) 102299, https://doi.org/10.1016/j.mtchem.2024.102299.
[8] M.G. Kotp, I.M. Minisy, B. Al-Saida, S.-W. Kuo, Kinetics and selectivity insights into carbon dioxide capture utilizing carboxymethyl cellulose-polypyrrole nanocomposites: screening of silane functionalization, Carbohydr. Polym. 356 (2025) 123399, https://doi.org/10.1016/j.carbpol.2025.123399.
[9] A. Muzaffar, M.B. Ahamed, C.M. Hussain, Green supercapacitors: latest developments and perspectives in the pursuit of sustainability, Renew. Sustain. Energy Rev. 195 (2024) 114324, https://doi.org/10.1016/j.rser.2024.114324.
[10] K. Dissanayake, D. Kularatna-Abeywardana, A review of supercapacitors: materials, technology, challenges, and renewable energy applications, J. Energy Storage 96 (2024) 112563, https://doi.org/10.1016/j.est.2024.11256.
[11] H.S. Biswas, A.K. Kundu, Hydrogenated diamond-like carbon (HDLC) as energy storage nanomaterials: a review, Energy Storage 7 (2025) e70191, https://doi.org/10.1002/est2.70191Digital.
[12] S. Mukhopadhyay, A.R. Kottaichamy, M.C. Devendrachari, R.M. Mendhe, H.M. N. Kotresh, C.P. Vinod, M.O. Thotiyl, Electrochemical energy storage in an organic supercapacitor via a non-electrochemical proton charge assembly, Chem. Sci. 15 (2024) 1726–1735, https://doi.org/10.1039/D3SC05639B.
[13] R. Gupta, A. Malik, K. Kumari, S.K. Singh, V. Vivier, P.C. Mondal, Metal-free platforms for molecular thin films as high-performance supercapacitors, Chem. Sci. 15 (2024) 8775–8785, https://doi.org/10.1039/D4SC00611A.
[14] M. Girirajan, A.K. Bojarajan, I.N. Pulidindi, K.N. Hui, S. Sangaraju, An insight into the nanoarchitecture of electrode materials on the performance of supercapacitors, Coord. Chem. Rev. 518 (2024) 216080, https://doi.org/10.1016/j.ccr.2024.216080.
[15] D. Malavekar, S. Pujari, S. Jang, S. Bachankar, J.H. Kim, Recent development on transition metal oxides-based core–shell structures for boosted energy density supercapacitors, Small (2024) 2312179, https://doi.org/10.1002/smll.202312179.
[16] M.G. Kotp, S.-W. Kuo, Selective capturing of the CO2 emissions utilizing ecological (3-Mercaptopropyl)trimethoxysilane-Coated porous organic polymers in composite materials, Polymers 13 (2024) 1759, https://doi.org/10.3390/polym16131759.
[17] D. Zhou, K. Zhang, S. Zou, X. Li, H. Ma, Conjugated microporous polymers: their synthesis and potential applications in flexible electrodes, J. Mater. Chem. A 12 (2024) 17021–17053, https://doi.org/10.1039/D4TA02085E.
[18] M. Shahmirzaee, A. Nagai, An appraisal for providing Charge Transfer (CT) through synthetic porous frameworks for their semiconductor applications, Small 20 (2024) 2307828, https://doi.org/10.1002/smll.202307828.
[19] A.O. Mousa, Z.-I. Lin, S.V. Chaganti, C.-H. Chuang, C.-K. Chen, S.-W. Kuo, M. G. Mohamed, Bifunctional imidazolium linked tetraphenylethene based conjugated microporous polymers for dynamic antibacterial properties and supercapacitor electrodes, Polym. Chem. 15 (2024) 397–411, https://doi.org/10.1039/D3PY01303K.
[20] N. Naz, M.H. Manzoor, S.M.G. Naqvi, U. Ehsan, M. Aslam, F. Verpoort, Porous organic polymers; an emerging material applied in energy, environmental and biomedical applications, Appl. Mater. Today 38 (2024) 102198, https://doi.org/10.1016/j.apmt.2024.102198.
[21] S. You, Z. Ding, R. Yuan, J. Long, C. Xu, Confined synthesis of conjugated microporous polymers for selective photocatalytic oxidation of amines, J. Colloid Interface Sci. 664 (2024) 63–73, https://doi.org/10.1016/j.jcis.2024.03.031.
[22] P.N. Singh, M.G. Mohamed, M.G. Kotp, T. Mondal, S.V. Chaganti, M. Ibrahim, S. U. Sharma, Y. Ye, S.-W. Kuo, Nitrogen-and sulfur-rich microporous carbons derived from conjugated microporous polymers for CO2 uptake, supercapacitor energy storage, and electrochemical hydrogen production, ACS Appl. Polym. Mater. 7 (2025) 3324–3336, https://doi.org/10.1021/acsapm.5c00012.
[23] M.G. Kotp, S.-W. Kuo, Engineering porous organic polymers for enhanced CO_2 capture: from synthesis to implementation, Chem. Sci. (2026), https://doi.org/10.1039/D6SC00384B.
[24] A.O. Mousa, M.G. Kotp, S.-W. Kuo, A sustainable bio-based benzoxazine porous organic polymer derived vanillin for synergistic catalysis: green synthesis of Pd nanoparticles and enhanced nitro reduction, Polymer (2026) 130126, https://doi.org/10.1016/j.polymer.2026.130126.
[25] Y. Gao, Q. Hui, Q. Liu, X. Xia, R. Li, Y. Chen, D. Wang, H. Liu, Insights into the heteroatom-incorporated storage mechanism of hierarchically interconnected porous conjugated polymer networks for extremely stable potassium-ion storage, Chem. Eng. J. 483 (2024) 149200, https://doi.org/10.1016/j.cej.2024.149200.
[26] D. Divya, H. Mishra, R. Jangir, Covalent organic frameworks and their composites as enhanced energy storage materials, Chem. Commun. 61 (2025) 2403–2423, https://doi.org/10.1039/D4CC04688A.
[27] N. An, M. Wei, C. Guo, J. Xin, C. Meng, D. Sun, Y. Lei, Z. Hu, X. Dong, L. Zhao, Integrated N-doped carbon electrodes with regional synergistic energy storage mechanisms for zinc-ion hybrid supercapacitors, J. Power Sources 599 (2024) 234212, https://doi.org/10.1016/j.jpowsour.2024.234212.
[28] A.O. Mousa, M.G. Mohamed, M.G. Kotp, S.-W. Kuo, Pyrazine-tethered conjugated microporous polymers for silver nanoparticle dispersion toward enhanced catalytic reduction of p-nitrophenol and p-fluoronitrobenzene, Eur. Polym. J. 248 (2026) 114599, https://doi.org/10.1016/j.eurpolymj.2026.114599.
[29] M.G. Kotp, M.G. Mohamed, S.-W. Kuo, Conjugated microporous polymer electrodes for supercapacitors: recent progress, key challenges, and future directions, Chem. Sci. 16 (2025) 20718–20754, https://doi.org/10.1039/D5SC05384F.
[30] L. Yang, X. Li, W. Huang, X. Rao, Y. Lai, Pharmacological properties of indirubin and its derivatives, Biomed. Pharmacother. 151 (2022) 113112, https://doi.org/10.1016/j.biopha.2022.113112.
[31] G.M. Cragg, P.G. Grothaus, D.J. Newman, Impact of natural products on developing new anti-cancer agents, Chem. Rev. 109 (2009) 3012–3043, https://doi.org/10.1021/cr900019j.
[32] C. Cunha, J. Sérgio Seixas de Melo, The molecules of colour. New structural derivatives from indigo: tryptanthrin and indirubin, 45 - 65, https://doi.org/10.1039/9781837672301, 2023.
[33] M.G. Kotp, A.F.M. EL-Mahdy, T.-L. Yang, S.-W. Kuo, A pyridinyl-phenanzine conjugated microporous polymer decorated with ultrafine Ag nanoparticles mediates the rapid reduction of nitrophenol, Microporous Mesoporous Mater. 331 (2022) 111669, https://doi.org/10.1016/j.micromeso.2021.111669.
[34] S. Yamazaki, K. Banno, Excited-state intramolecular proton transfer toward conical intersections in indigo, epindolidione, and indirubin, J. Phys. Chem. A . 128 (2024) 6351–6361, https://doi.org/10.1021/acs.jpca.4c01804.
[35] D.C. Nobre, E. Delgado-Pinar, C. Cunha, A.M. Galvao, J.S.S. de Melo, Indirubin: nature finding efficient light-activated protective molecular mechanisms, Dyes Pigm 212 (2023) 111116, https://doi.org/10.1016/j.dyepig.2023.111116.
[36] K.-Y. Choi, A review of recent progress in the synthesis of bio-indigoids and their biologically assisted end-use applications, Dyes Pigm 181 (2020) 108570, https://doi.org/10.1016/j.dyepig.2020.108570.
[37] M.G. Kotp, J. Lüder, S.-W. Kuo, A.F.M. EL-Mahdy, Phenazine-integrated conjugated microporous polymers for modulating the mechanics of supercapacitor electrodes, Mater. Adv. 5 (2024) 4142–4150, https://doi.org/10.1039/D3MA00979C.
[38] M.G. Kotp, S.-W. Kuo, A.F.M. EL-Mahdy, Phenazine-based conjugated microporous polymers: influence of planarity and imine content on energy storage performance, Colloids Surf. A Physicochem. Eng. Asp. 685 (2024) 133210, https://doi.org/10.1016/j.colsurfa.2024.133210.
[39] M.G. Kotp, S.U. Sharma, J.-T. Lee, A.F.M. EL-Mahdy, S.-W. Kuo, Triphenylamine-based conjugated microporous polymers as dye adsorbents and supercapacitors, J. Taiwan Inst. Chem. Eng. 134 (2022) 104310, https://doi.org/10.1016/j.jtice.2022.104310.
[40] M.G. Kotp, N.L. Torad, H. Nara, W. Chaikittisilp, J. You, Y. Yamauchi, A.F.M. EL-Mahdy, S.-W. Kuo, Tunable thiophene-based conjugated microporous polymers for the disposal of toxic hexavalent chromium, J. Mater. Chem. A 11 (2023) 15022–15032, https://doi.org/10.1039/D3TA00175J.
[41] C. Wang, J. Yan, M. Du, J.A. Burlison, C. Li, Y. Sun, D. Zhao, J. Liu, One step synthesis of indirubins by reductive coupling of isatins with KBH4, Tetrahedron 73 (2017) 2780–2785, https://doi.org/10.1016/j.tet.2017.03.077.
[42] M.G. Kotp, A.M. Elewa, A.F.M. EL-Mahdy, H.-H. Chou, S.-W. Kuo, Tunable pyridyl-based conjugated microporous polymers for visible light-driven hydrogen evolution, ACS Appl. Energy Mater. 4 (2021) 13140–13151, https://doi.org/10.1021/acsaem.1c02772.
[43] M.G. Mohamed, A.F.M. EL-Mahdy, M.G. Kotp, S.-W. Kuo, Advances in porous organic polymers: syntheses, structures, and diverse applications, Mater. Adv. 3 (2022) 707–733, https://doi.org/10.1039/D1MA00771H.
[44] W. Liu, S.-D. Jiang, Y. Yan, W. Wang, J. Li, K. Leng, S. Japip, J. Liu, H. Xu, Y. Liu, I.-H. Park, I.-H. Park, Y. Bao, W. Yu, M.D. Guiver, S. Zhang, K.P. Loh, A solution-processable and ultra-permeable conjugated microporous thermoset for selective hydrogen separation, Nat. Commun. 11 (2020) 1–8, https://doi.org/10.1038/s41467-020-15503-6.
[45] T.-M. Geng, D.-K. Li, Z.-M. Zhu, W.-Y. Zhang, S.-N. Ye, H. Zhu, Z.-Q. Wang, Fluorescent conjugated microporous polymer based on perylene tetraanhydride bisimide for sensing o-nitrophenol, Anal. Chim. Acta 1011 (2018) 77–85, https://doi.org/10.1016/j.aca.2018.01.002.
[46] M. Karabacak, E. Kose, A. Atac, E. Sas, A. Asiri, M. Kurt, Experimental (FT-IR, FT-Raman, UV–Vis, 1H and 13C NMR) and computational (density functional theory) studies on 3-bromophenylboronic acid, J. Mol. Struct. 1076 (2014) 358–372, https://doi.org/10.1016/j.molstruc.2014.07.058.
[47] D. Kong, Z. Xiao, Y. Gao, X. Zhang, R. Guo, X. Huang, X. Li, L. Zhi, Sp2-carbon dominant carbonaceous materials for energy conversion and storage, Mater. Sci. Eng. R Rep. 137 (2019) 1–37, https://doi.org/10.1016/j.mser.2018.10.001.
[48] T.F. Qahtan, T.O. Owolabi, S. Alotibi, F.S. Alhakami, T.A. Saleh, Reduction of graphene oxide film on glass substrate using argon ion beam irradiation: a systematic study with X-ray photoelectron spectroscopy analysis, J. Mol. Struct. 1312 (2024) 138630, https://doi.org/10.1016/j.molstruc.2024.138630.
[49] S. Wu, D. Wang, C. Liu, G. Fang, T.-R. Sun, P. Cui, H. Yan, Y. Wang, D. Zhou, Pyridinic-and pyrrolic nitrogen in pyrogenic carbon improves electron shuttling

during microbial Fe (III) reduction, ACS Earth Space Chem. 5 (2021) 900–909, https://doi.org/10.1021/acsearthspacechem.1c00012.
[50] Z.X. Wang, J.C. Zhang, W.L. Cao, Study on the Cation-π interactions between ammonium ion and aromatic π systems, Chin. J. Chem. 24 (2006) 1523–1530, https://doi.org/10.1002/cjoc.200690287.
[51] X.-C. Li, Y. Zhang, C.-Y. Wang, Y. Wan, W.-Y. Lai, H. Pang, W. Huang, Redox-active triazatruxene-based conjugated microporous polymers for high-performance supercapacitors, Chem. Sci. 8 (2017) 2959–2965, https://doi.org/10.1039/C6SC05532J.
[52] H. Jiang, L. Liu, K. Zhao, Z. Liu, X. Zhang, S. Hu, Effect of pyridinic-and pyrrolic-nitrogen on electrochemical performance of Pd for formic acid electrooxidation, Electrochim. Acta 337 (2020) 135758, https://doi.org/10.1016/j.electacta.2020.135758.
[53] M. Ejaz, M.G. Mohamed, M.G. Kotp, A.M. Elewa, S.-W. Kuo, Triphenylamine-linked triazine (DA) units based hypercrosslinked porous polymer: rapid adsorption and enhanced photodegradation of organic dyes from water, Colloids Surf. A Physicochem. Eng. Asp. 722 (2025) 137239, https://doi.org/10.1016/j.colsurfa.2025.137239.
[54] M.G. Kotp, S.-W. Kuo, Enhanced electrochemical performance of polyaniline and hyper-crosslinked porous polymer composite for advanced supercapacitor applications, Electrochim. Acta 531 (2025) 146440, https://doi.org/10.1016/j.electacta.2025.146440.
[55] F. Vilela, K. Zhang, M. Antonietti, Conjugated porous polymers for energy applications, Energy Environ. Sci. 5 (2012) 7819–7832, https://doi.org/10.1039/C2EE22002D.
[56] H. Liu, Z. Xu, J. Zhang, L. Rao, Y. Ge, Z.A. Xia, X. Zhang, L. Jiang, Y. Yi, B. Yang, Integrating strong luminescence and high mobility in organic single crystals of covalent pyrene dimers, Adv. Mater. 37 (2025) 2419981, https://doi.org/10.1002/adma.202419981.
[57] J. Li, K. Ge, A.O. Grammenos, P.L. Taberna, P. Simon, M. Antonietti, M. Odziomek, Understanding multi-stage charge storage on nanoporous carbons in zn-ion hybrid capacitors, Adv. Mater. (2025) 2502422, https://doi.org/10.1002/adma.202502422.
[58] Q. Liu, T. Wang, D. Jia, P. Ren, D. Wu, A refined stepwise carbonation strategy for controllable synthesis of porous carbon for high-performance zinc-ion hybrid capacitors, Adv. Funct. Mater. (2025) 2500016, https://doi.org/10.1002/adfm.202500016.
[59] J. Yang, H. You, Y. Han, H. Chen, K. Zhang, Y. Li, J. Bao, X. Ge, G. Pan, R. Xing, Synthesis of sulfonyl two-dimensional covalent organic frameworks for supercapacitor applications, ACS Appl. Mater. Interfaces 17 (2025) 11027–11035, https://doi.org/10.1021/acsami.4c22093.
[60] H. Zhuo, M. Zhang, H. Zhang, H. Lin, G. Yang, S. Tao, C. Zheng, X. Zhang, Modified triphenylamine donors with shallower HOMO energy levels to construct long-wavelength TADF emitters of efficient organic light-emitting diodes, Chin. Chem. Lett. 36 (2025) 110760, https://doi.org/10.1016/j.cclet.2024.110760.
[61] L. Xie, F. Su, L. Xie, X. Guo, Z. Wang, Q. Kong, G. Sun, A. Ahmad, X. Li, Z. Yi, Effect of pore structure and doping species on charge storage mechanisms in porous carbon-based supercapacitors, Mater. Chem. Front. 4 (2020) 2610–2634, https://doi.org/10.1039/D0QM00180E.
[62] M.G. Kotp, N.L. Torad, J. Lüder, A. El-Amir, W. Chaikittisilp, Y. Yamauchi, A.F. M. EL-Mahdy, A phenazine conjugated microporous polymer-based quartz crystal microbalance for sensitive detection of formaldehyde vapors at room temperature: an experiment and density functional theory study, J. Mater. Chem. A 11 (2023) 764–774, https://doi.org/10.1039/D2TA07966F.
[63] P. Wu, J. Wang, Y. Li, C. He, Z. Xie, C. Duan, Luminescent sensing and catalytic performances of a multifunctional lanthanide-organic framework comprising a triphenylamine moiety, Adv. Funct. Mater. 21 (2011) 2788–2794, https://doi.org/10.1002/adfm.201100115.
[64] A. Iwan, D. Sek, Polymers with triphenylamine units: photonic and electroactive materials, Prog. Polym. Sci. 36 (2011) 1277–1325, https://doi.org/10.1016/j.progpolymsci.2011.05.001.
[65] W. Zhang, P. Liu, A. Sadollahkhani, Y. Li, B. Zhang, F. Zhang, M. Safdari, Y. Hao, Y. Hua, L. Kloo, Investigation of triphenylamine (TPA)-based metal complexes and their application in perovskite solar cells, ACS Omega 2 (2017) 9231–9240, https://doi.org/10.1021/acsomega.7b01434.